INTERNATIONAL JOURNAL FOR NUMERICAL METHODS IN FLUIDS, VOL. 5, 133–154 (1985)

NUMERICAL STUDY OF THERMAL CONVECTION IN ROTATING CHANNEL FLOW

SIVAGNANAM THANGAM AND CHARLES G. SPEZIALE

Stevens Institute of Technology, Hoboken, N.J. 07030, U.S.A.

SUMMARY

A numerical study is conducted on the effect of sidewall heating in the pressure-driven laminar flow of an incompressible viscous fluid through a rectangular channel that is subjected to a spanwise rotation. The time-dependent Navier–Stokes equations are solved along with the conservation equations for energy and mass by a finite-difference technique. The effect of weak to moderate sidewall heating on the overall flow structure at different rotation rates is studied. It is observed that for weak sidewall heating, the secondary flow structure is quite similar to the corresponding isothermal case. However, when the sidewall heating is moderate, various types of secondary flow fields are found to occur depending on the magnitude of the rotation. The influence of rotational speed on the net heat transport for different levels of sidewall heating is also studied. It is found that when the sidewall heating is weak, the basic secondary flow structure for the non-rotating case is of a unicellular form and an increase in the rotation speed leads to an increase in the net heat transfer due mainly to the rotationally driven transport of fluid from the high temperature to the low temperature region. On the other hand, when the sidewall heating is moderate so that the basic secondary flow structure for the non-rotating case has a multicellular configuration, an increase in the rotation speed leads to a decrease in the heat transport due to the weakening of the shear layer near the hot wall.

KEY WORDS Thermal Convection Rotating Channel Flow Finite Difference Method Secondary Flows Rotational Instabilities

INTRODUCTION

The analysis of non-isothermal viscous flow through channels driven by an axial pressure gradient has been a subject of considerable interest to scientists and engineers as a result of its ubiquitous occurrence in a variety of engineering applications. For example, in the design of micro-electronic equipment, heat transfer from large scale integrated circuits to the cooling fluid in typical designs can essentially be thought of as combined laminar free and forced convection in a horizontal channel.[1,2] Flow fields in a number of active and passive solar energy collectors also fall into this category. Convective heat transport in a variety of heat exchange equipment is another example where, under certain conditions, non-isothermal laminar viscous flow modelling is of use.[1] In this context, we can isolate a class of heat transport problems that occur in channels or in ducts with a large aspect ratio (i.e. height to width ratio; see Figure 1) due to heated side walls. Here again, the case of pressure-driven viscous flow in curved channels with a heated sidewall is of particular interest owing to its common occurrence in a wide variety of heat exchange devices. Another interesting case of sidewall heating occurs in channel flows that are subjected to a spanwise rotation. Of course, the importance of an analysis of such problems is tied to its use in the prediction of cooling requirements for the rotor blades in gas turbines and other rotating

0271–2091/85/02 0133–22$02.20

Received 19 December 1983
Revised 13 April 1984

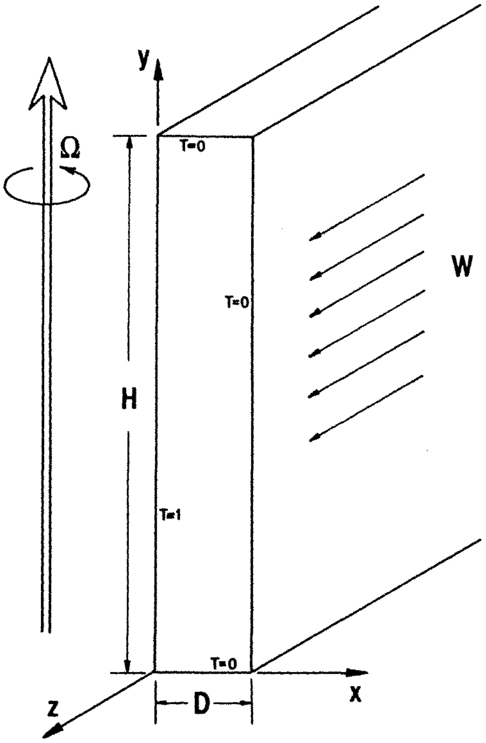

Figure 1. The flow configuration

machinery,[3,4] its relevance to a variety of geophysical problems,[5,6] and its qualitative similarity to the flow field in channels with a large radius of curvature.[7]

In this paper we will conduct a numerical study on the effect of sidewall heating in laminar pressure-driven flow through rectangular channels subjected to a steady spanwise rotation. The case of pressure-driven isothermal viscous flows in channels subjected to a steady spanwise rotation has been a topic of considerable interest to researchers, and a detailed discussion of the secondary flow structure and instabilities in the form of longitudinal roll-cells can be found in References 8–11. In the present paper we will examine the effect of sidewall heating on rotating channel flows. Consequently, we have maintained the aspect ratio of the channel and the Reynolds number of the flow to be constant. The particular values chosen were those that were used in the corresponding isothermal flow situation studied by Speziale and Thangam.[11] Hence, a basis for comparison is established.

The present work can be thought of as consisting of two parts. In the first part, we examine the effect of sidewall heating on the secondary flow structure for three different rotation rates. The values of the selected rotation rates correspond to zero rotation, moderate rotation, and rapid rotation. We note here that the secondary flow structure in the interior portion of the channel for the corresponding isothermal flow situation[11] was found to be in the form of longitudinal roll-cells if the rotation rate was moderate, and in the form of a Taylor–Proudman configuration when the rotation rate was large. Furthermore, it is well known that when a stationary channel of large aspect ratio with a quiescent fluid is subjected to increasing values of the sidewall temperature differential, the basic unicellular flow pattern breaks down into a multi-cellular form.[12] Thus, to analyse the effect of sidewall heating, two levels of temperature differentials were used: one in which the secondary flow field for the non-rotating case showed a unicellular pattern, and the other in which the more complex multi-cellular pattern was present. In this manner, it was felt that a clear understanding of the combined influence of the buoyancy and the Coriolis effects on the structure of the secondary flow field may be obtained. The full non-linear Navier–Stokes equations with the Boussinesq approximation are solved along with the energy equation by a finite difference method. Both the secondary flow field structure in the form of streamlines and isotherms, as well as the profiles of the axial velocity and temperature are presented for the cases mentioned above.

In the second part of this paper, computations were carried out to study the influence of the rotational speed of the channel on the net amount of heat transferred at different levels of sidewall heating. This is of particular use in the prediction of cooling rate requirements for rotating machinery and other heat exchange equipment. To the best knowledge of the authors, these calculations constitute the first numerical study where the combined influences of the convective, buoyancy and Coriolis effects are analysed in the specified flow configuration. Although the study itself is by no means exhaustive, the authors believe that it can provide some insight for the analysis of this intriguing phenomenon in problems of engineering importance.

FORMULATION OF THE PHYSICAL PROBLEM

The laminar pressure driven flow of an incompressible viscous fluid through a straight rectangular channel subjected to a steady spanwise rotation and lateral heating is considered (see figure 1). The axial pressure gradient $\partial P/\partial z = -G$ is constant (where P is the modified pressure which includes the gravitational and centrifugal force potentials) and is maintained by external means. The walls of the channel are each maintained at a uniform temperature and a temperature difference of ΔT exists between the lateral walls. The channel is sufficiently long so that there exists an interior portion where end effects are absent and the flow properties are independent of the axial coordinate z. In the absence of rotation and heating, the fully-developed velocity field $\mathbf{V}$ is of the unidirectional form

$$\mathbf{V} = w(x, y)\mathbf{k} \tag{1}$$

where w may be determined from the Poisson equation[13]

$$\nabla^2 w = -G/\mu \tag{2}$$

Here, μ is the dynamic viscosity of the fluid. Equation (2) is solved subject to the no-slip condition that w vanishes on the walls of the channel which yields the classical quasi-parabolic velocity profile. For small to moderate variations in temperature, the equation of state for the fluid can be written as

$$\rho = \rho_r[1 - \beta(T - T_r)] \tag{3}$$

where

$$\beta = -\frac{1}{\rho_r}\left(\frac{\partial \rho}{\partial T}\right)_P$$

is the coefficient of thermal expansion. The subscript r indicates a suitable reference state, and the temperature and density are represented, respectively, by T and ρ.

The continuity equation, momentum equation and the transport equation of heat for an incompressible fluid with the Boussinesq approximation (valid for weak to moderate heating) are

$$\nabla \cdot \mathbf{V} = 0 \tag{4}$$

$$\partial_t \mathbf{V} + \mathbf{V}\cdot\nabla\mathbf{V} = -\frac{1}{\rho_r}\nabla \mathrm{P} + \nu\nabla^2\mathbf{V} - 2\mathbf{\Omega}\times\mathbf{V} - \{\beta(T - T_r)\}\mathbf{g} \tag{5}$$

$$\partial_t T + \mathbf{V}\cdot\nabla T = \alpha\nabla^2 T \tag{6}$$

In this set of equations, the vector $\mathbf{V} = \{u(x, y, t), v(x, y, t), w(x, y, t)\}$ is the velocity (where u and v constitute the secondary flow components), $\mathbf{g} = \{0, -g, 0\}$ is the acceleration due to gravity, and t is the time. The thermal diffusivity and the kinematic viscosity are represented by α and ν respectively. For the problem under consideration (relative to an observer who is rotating with the channel at an angular velocity $\mathbf{\Omega} = \Omega\mathbf{j}$), equations (4)–(6) take the following form:

$$\partial_x u + \partial_y v = 0 \tag{7}$$

$$\partial_t u + u\partial_x u + v\partial_y u = -\frac{1}{\rho_r}\partial_x P + \nu\nabla^2 u - 2\Omega w \tag{8}$$

$$\partial_t v + u\partial_x v + v\partial_y v = -\frac{1}{\rho_r}\partial_y P + \nu\nabla^2 v + g\beta(T - T_r) \tag{9}$$

$$\partial_t w + u\partial_x w + v\partial_y w = \frac{1}{\rho_r}G + \nu\nabla^2 w + 2\Omega u \tag{10}$$

$$\partial_t T + u\partial_x T + v\partial_y T = \alpha\nabla^2 T \tag{11}$$

where $\nabla^2 = \partial_x^2 + \partial_y^2$ is the two-dimensional Laplacian. In formulating (7)–(11) we have made use of the fact that the velocity and temperature are independent of the axial co-ordinate z.

A stream function ψ for the secondary flow exists so that

$$u = -\partial_y\psi, \quad v = \partial_x\psi \tag{12}$$

In (12), ψ is a solution of the Poisson equation

$$\nabla^2\psi = \omega \tag{13}$$

where

$$\omega = \partial_x v - \partial_y u$$

is the axial component of the vorticity, which is determined from the z component of the vorticity transport equation given by

$$\partial_t\omega + u\partial_x\omega + v\partial_y\omega = \nu\nabla^2\omega + 2\Omega\partial_y w + g\beta\partial_x T \tag{14}$$

As a consequence of (13), it is clear that the secondary flows result from a non-zero axial vorticity ω. Furthermore, from (14) we see that the body force terms (i.e. the Coriolis term $2\Omega\partial_y w$ and the buoyancy term $g\beta\partial_x T$) serve as sources for the axial vorticity, and thus are the driving mechanism for the creation of secondary flows. For the purposes of analysis it is convenient to cast the variables in their dimensionless form with the scaling parameters D for length, W_0 for velocity and ΔT for temperature which are, respectively, the width of the channel, the integrated average axial velocity for the non-rotating case, and the temperature difference between the sidewalls. In dimensionless form, the governing equations to be solved are as follows:

$$\partial_t w + u\partial_x w + v\partial_y w = C + \frac{1}{Re}\nabla^2 w + \frac{1}{Ro}u \tag{15a}$$

$$\partial_t\omega + u\partial_x\omega + v\partial_y\omega = \frac{1}{Re}\nabla^2\omega + \frac{1}{Ro}\partial_y w + (Ra/PrRe^2)\partial_x T \tag{15b}$$

$$\partial_t T + u\partial_x T + v\partial_y T = (1/RePr)\nabla^2 T \tag{15c}$$

$$\nabla^2 \psi = \omega \tag{15d}$$

$$u = -\partial_y \psi, \quad v = \partial_x \psi \tag{15e}$$

where

$C = GD/(\rho W_0^2)$ is the dimensionless pressure gradient
$Re = W_0 D/\nu$ is the Reynolds number
$Ro = W_0/(2\Omega D)$ is the Rossby number
$Pr = \nu/\alpha$ is the Prandtl number
$Ra = g\beta\Delta T D^3/(\nu\alpha)$ is the Rayleigh number

The coupled system of non-linear partial differential equations (15) is solved subject to the boundary conditions

$$\begin{aligned} &u=0, \quad v=0, \quad w=0, \quad \psi=0, \quad T=0 \quad \text{at } (x,0),\ (x,A),\ (1,y) \\ &u=0, \quad v=0, \quad w=0, \quad \psi=0, \quad T=1 \quad \text{at } (0,y) \end{aligned} \tag{16}$$

on the walls of the channel. Here, $A = H/D$ is the aspect ratio of the channel. The boundary conditions for axial vorticity, however, must be derived by a Taylor expansion. This will be discussed later.

The initial conditions for the case being considered are those corresponding to fully-developed laminar flow in a stationary channel which is subjected to an impulsively applied angular velocity and lateral temperature difference. Hence, we have

$$u=0, \quad v=0, \quad w=w_0, \quad \omega=0, \quad \psi=0, \quad T=0 \quad \text{at } t=0 \tag{17}$$

where w_0 is the classical quasi-parabolic velocity profile obtained from (2).

METHOD OF SOLUTION

A finite-difference procedure where the cross-section of the channel is discretized into an $M \times N$ rectangular grid is used to solve the governing equations (15a)–(15e) subject to the boundary and initial conditions given by (16) and (17). In this approach, the convective terms and the diffusion terms in (15a)–(15c) are, respectively, formulated by Arakawa's scheme and the Dufort–Frankel scheme.[14] This approach is advantageous since it constitutes a conservative explicit difference scheme which has no boundary condition problems.[14] Arakawa's scheme, for the limit of pure convection in this problem, conserves ω, ω^2, w, w^2, T and T^2 (as well as the total kinetic energy) and is, thus, not subject to non-linear instabilities that arise from aliasing errors.[14] The governing equations (15) take the finite difference form

$$\left(\frac{\mathrm{D}w}{\mathrm{D}t}\right)^n_{i,j} = C + \frac{1}{Re}\left[\frac{w^n_{i+1,j} - w^{n-1}_{i,j} - w^{n+1}_{i,j} + w^n_{i-1,j}}{(\Delta x)^2} + \frac{w^n_{i,j+1} - w^{n-1}_{i,j} - w^{n+1}_{i,j} + w^n_{i,j-1}}{(\Delta y)^2}\right] + \frac{1}{Ro}u^n_{i,j} \tag{18a}$$

$$\begin{aligned} \left(\frac{\mathrm{D}\omega}{\mathrm{D}t}\right)^n_{i,j} = {} & \frac{1}{Re}\left[\frac{\omega^n_{i+1,j} - \omega^{n-1}_{i,j} - \omega^{n+1}_{i,j} + \omega^n_{i-1,j}}{(\Delta x)^2} + \frac{\omega^n_{i,j+1} - \omega^{n-1}_{i,j} - \omega^{n+1}_{i,j} + \omega^n_{i,j-1}}{(\Delta y)^2}\right] \\ & + \frac{1}{Ro}\left[\frac{w^n_{i,j+1} - w^n_{i,j-1}}{2\Delta y}\right] + \left(\frac{Ra}{PrRe^2}\right)\left[\frac{T^n_{i+1,j} - T^n_{i-1,j}}{2\Delta x}\right] \end{aligned} \tag{18b}$$

$$\left(\frac{\mathrm{D}T}{\mathrm{D}t}\right)^n_{i,j} = \left(\frac{1}{RePr}\right)\left[\frac{T^n_{i+1,j} - T^{n-1}_{i,j} - T^{n+1}_{i,j} + T^n_{i-1,j}}{(\Delta x)^2} + \frac{T^n_{i,j+1} - T^{n-1}_{i,j} - T^{n+1}_{i,j} + T^n_{i,j-1}}{(\Delta y)^2}\right]$$

$$\frac{\psi^n_{i+1,j}-2\psi^n_{i,j}+\psi^n_{i-1,j}}{(\Delta x)^2}+\frac{\psi^n_{i,j+1}-2\psi^n_{i,j}+\psi^n_{i,j-1}}{(\Delta y)^2}=\omega^n_{i,j} \tag{18c}$$

$$u^n_{i,j}=-\left(\frac{\psi^n_{i,j+1}-\psi^n_{i,j-1}}{2\Delta y}\right) \tag{18d}$$

$$v^n_{i,j}=\frac{\psi^n_{i+1,j}-\psi^n_{i-1,j}}{2\Delta x} \tag{18e}$$

As indicated earlier, Arakawa's method will be used to formulate the convective derivatives in (18a)–(18c). In Arakawa's method, consistent with the stream function definition given by (15e), the convective derivative of any field variable Φ is represented as follows:

$$\begin{aligned}\left(\frac{\mathrm{D}\Phi}{\mathrm{D}t}\right)^n_{i,j} &\equiv (\partial_t\Phi+u\partial_x\Phi+v\partial_y\Phi)^n_{i,j}\\ &=\frac{\Phi^{n+1}_{i,j}-\Phi^{n-1}_{i,j}}{2\Delta t}+\frac{1}{12\Delta x\Delta y}[(\psi^n_{i+1,j}-\psi^n_{i-1,j})(\Phi^n_{i,j+1}-\Phi^n_{i,j-1})\\ &\quad-(\psi^n_{i,j+1}-\psi^n_{i,j-1})(\Phi^n_{i+1,j}-\Phi^n_{i-1,j})+\psi^n_{i+1,j}(\Phi^n_{i+1,j+1}-\Phi^n_{i+1,j-1})\\ &\quad-\psi^n_{i-1,j}(\Phi^n_{i-1,j+1}-\Phi^n_{i-1,j-1})-\psi^n_{i,j+1}(\Phi^n_{i+1,j+1}-\Phi^n_{i-1,j+1})\\ &\quad+\psi^n_{i,j-1}(\Phi^n_{i+1,j-1}-\Phi^n_{i-1,j-1})+\Phi^n_{i,j+1}(\psi^n_{i+1,j+1}-\psi^n_{i-1,j+1})\\ &\quad-\Phi^n_{i,j-1}(\psi^n_{i+1,j-1}-\psi^n_{i-1,j-1})-\Phi^n_{i+1,j}(\psi^n_{i+1,j+1}-\psi^n_{i+1,j-1})\\ &\quad+\Phi^n_{i-1,j}(\psi^n_{i-1,j+1}-\psi^n_{i-1,j-1})]\end{aligned} \tag{19}$$

In (18) and (19), Δx and Δy are, respectively, the grid lengths in the x and y directions, Δt is the time interval, and, thus, for any field variable Φ

$$\Phi^n_{i,j}\equiv\Phi(i\Delta x, j\Delta y, n\Delta t),\quad n=0,1,\cdots;\quad i=0,1,\cdots,M;\quad j=0,1,\cdots,$$

Equations (18) in conjunction with (19) represent the complete finite-difference formulation of the governing equations of motion (15). These equations are supplemented with the boundary conditions (16) and the initial conditions (17). To obtain the boundary conditions for the axial vorticity, a second-order accurate Taylor expansion of (15d) in the vicinity of the walls of the channel is employed. This yields the following boundary conditions:

$$\begin{aligned}\omega^n_{0,j}&=\frac{8\psi^n_{1,j}-\psi^n_{2,j}}{2(\Delta x)^2},\quad \omega^n_{M,j}=\frac{8\psi^n_{M-1,j}-\psi^n_{M-2,j}}{2(\Delta x)^2}\\ \omega^n_{i,0}&=\frac{8\psi^n_{i,1}-\psi^n_{i,2}}{2(\Delta y)^2},\quad \omega^n_{i,N}=\frac{8\psi^n_{i,N-1}-\psi^n_{i,N-2}}{2(\Delta y)^2}\end{aligned} \tag{20}$$

The solution procedure is as follows: using the initial values, the updated values of w, ω and T are obtained from (18a)–(18c). The solution to (18d) is then obtained using a compact non-iterative Poisson solver due to Buneman[15] which employs cyclic reduction. The boundary conditions on ω are then updated using (20), and the entire procedure is repeated until a steady-state is obtained. To ensure numerical stability, a stability criterion obtained through a simple superposition of the von Neumann stability condition and the generalized CFL condition was used; Δt then has to satisfy the constraint

$$\Delta t\leqslant\left[\frac{2}{Re}\left\{\frac{1}{(\Delta x)^2}+\frac{1}{(\Delta y)^2}\right\}+\frac{|u|_{\max}}{\Delta x}+\frac{|v|_{\max}}{\Delta y}\right]^{-1} \tag{21}$$

In practice, this constraint was applied with a safety factor of about two. The formulation of this problem, in its entirety, is second-order accurate, i.e. the truncation error τ goes as

$$\| \tau \| = O(\Delta x^2, \Delta y^2, \Delta t^2) \tag{22}$$

where $\| \cdot \|$ denotes any suitable norm. Unfortunately, because of the complex non-linear nature of the governing equations, formal error estimates are not available. In all of the calculations to be presented here, a 16×128 finite difference grid was used which was found to be more than adequate to pick up the rapid variations in the fields which occur near the upper and lower walls of the channel.

RESULTS AND DISCUSSION

Since the aim of this work was primarily to study the influence of sidewall heating on incompressible viscous flow in rotating rectangular channels, for convenience, both the Reynolds number and the aspect ratio of the channel were kept constant at values of 270 and 8, respectively. These numbers were chosen chiefly because they correspond to those used earlier by previous researchers[10,11] to analyse isothermal viscous flows in rotating rectangular channels. In this manner, it was felt that a clear understanding of the influence of sidewall heating coupled with rotational effects could be obtained. As indicated earlier, within a qualitative framework, the flow in a rotating channel is analogous to the flow in a stationary channel with a large radius of curvature. Consequently, the results to be discussed here can be of some use in analysing heat transport in curved channels subjected to wall heating which is also a common occurrence in a variety of engineering applications.

For the purposes of discussion, the results may be grouped into the following three categories in terms of the rotation rates: zero rotation, moderate rotation and strong rotation. For each of these three cases we consider both moderate and weak sidewall heating. Hence, the Boussinesq approximation applies to all of the cases considered. For the weak heating case, the thermal Rayleigh number Ra was maintained at $1{\cdot}1 \times 10^5$ in all the results under discussion. However, in the results for the moderate heating case, a value of $Ra = 4{\cdot}4 \times 10^5$ was chosen when the channel was subjected to a spanwise rotation, whereas a value of $Ra = 5{\cdot}4 \times 10^5$ was chosen for the non-rotating case. The choice of these values of Ra was made primarily because they provide a suitable illustration of the evolution of the secondary flow.

We first consider the results shown in Figures 2–9 which represent the non-rotating case (i.e. $Ro = \infty$). The results shown in Figure 2–5 correspond to the weak heating case, whereas those in Figures 6–9 represent the moderate heating case. In Figures 2 and 3, computer generated contour maps of the streamlines for the secondary flow and the isotherms are shown at various time levels. Here, and in all the subsequent contour maps, the vertical boundary on the left side represents the hot wall; furthermore, in each plot, eight isopleths at equal intervals between the maximum and the minimum value are shown. As it may be seen from Figure 2, the fully developed configuration of the secondary flow is unicellular in nature. Examination of the isotherms shown in Figure 3 also clearly points to the fact that the fluid near the hot wall is merely swept up by the buoyancy effect and as the fluid comes in contact with the cold wall, it starts to sink, thus establishing the unicellular pattern. In Figure 4 the axial velocity profiles along the vertical centreline and along the horizontal centreline are plotted. These are approximately symmetrical w.r.t. both the vertical and the horizontal axis at the centre of the channel. In Figure 5 the temperature profiles along the vertical centreline and along the horizontal centreline of the channel are shown. In both Figures, the effect of buoyancy can be clearly seen.

Figures 6 and 7 depict the computer generated contour maps of the streamlines and isotherms for moderate heating in the absence of rotation. A comparison of Figures 2(b)–(d) and Figures

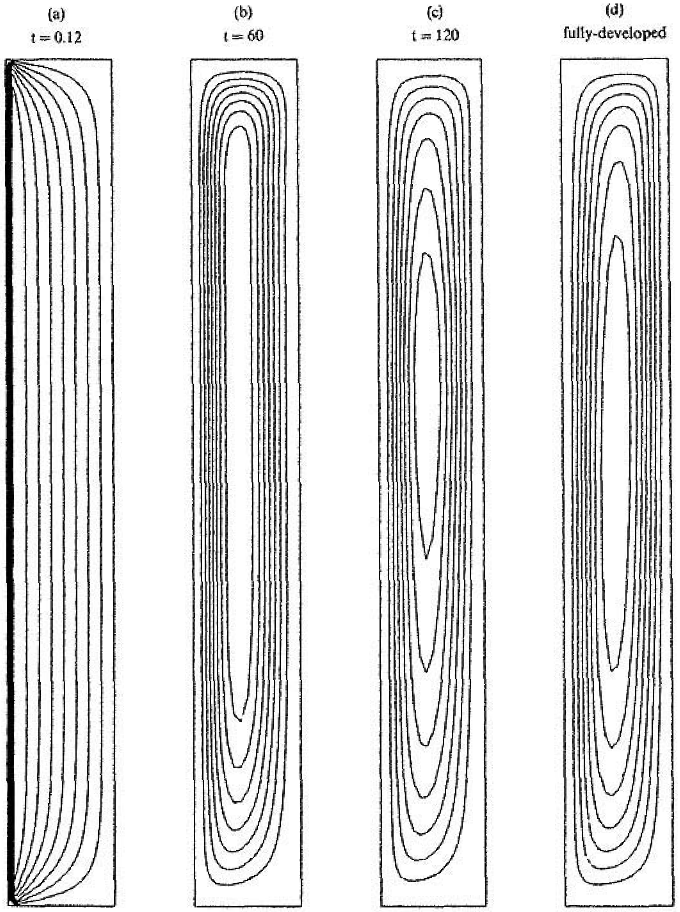

Figure 2. Contour maps of the secondary flow streamlines ($H/D = 8$, $Re = 270$, $Ra = 1{\cdot}09 \times 10^5$, $Ro = \infty$): (a) $t = 0{\cdot}12$; (b) $t = 60$; (c) $t = 120$; (d) fully-developed

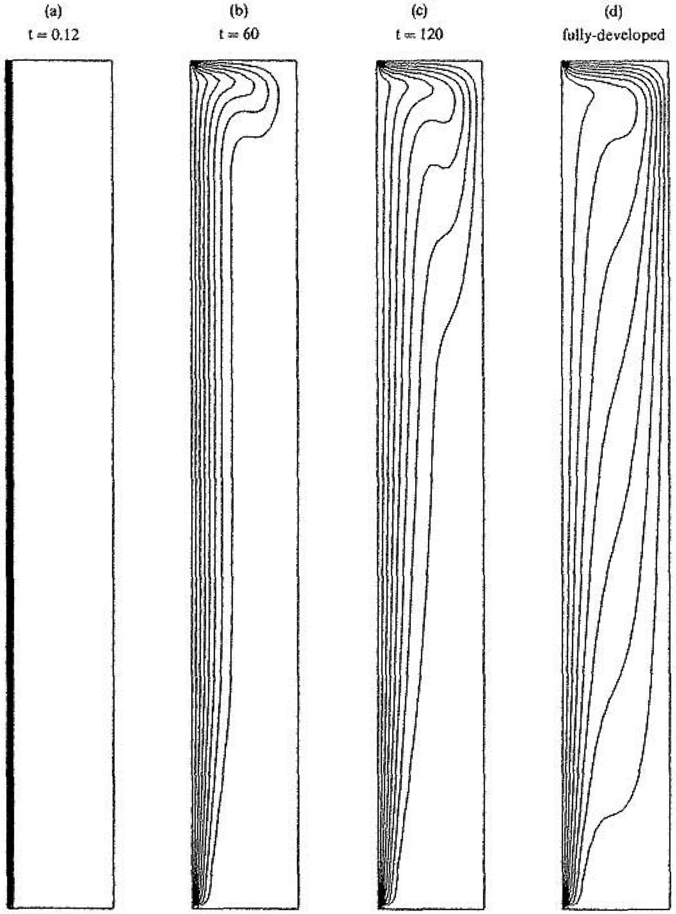

Figure 3. Contour maps of the isotherms. (Physical parameters are the same as shown in Figure 2)

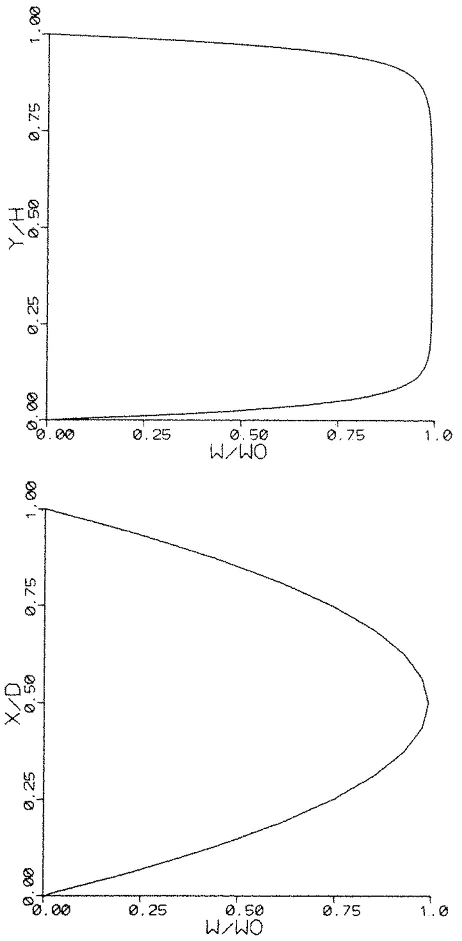

Figure 4. Fully-developed axial velocity profiles in the channel: (top) along the vertical centreline; (bottom) along the horizontal centreline

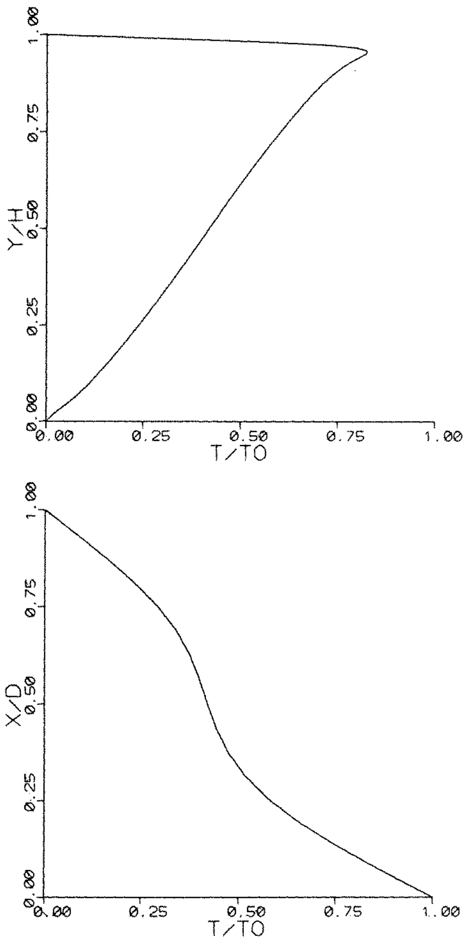

Figure 5. Fully-developed temperature profiles in the channel: (top) along the vertical centreline; (bottom) along the horizontal centreline. (Physical parameters are the same as shown in Figure 2.)

6(b)–(d) reveals that the single cell structure of the secondary flow at lower Rayleigh numbers breaks down with an increase in Rayleigh number to yield a multicellular pattern. The asymmetry introduced by the buoyancy effects, of course, will tend to sweep the cells upward near the heated wall, as seen from the fully developed streamlines in Figure 6(d). The influence of the multicellular secondary flow on the temperature field can also be seen from the isotherms corresponding to the fully developed case shown in Figure 7(d). In Figure 8, the axial velocity profiles along the vertical and horizontal centrelines are shown. Whereas the axial velocity profile is approximately symmetrical along the horizontal centreline, the axial velocity profile along the vertical centreline has a distinctive wavy shape. The results indicate that the locations of peaks and troughs in the top part of Figure 8 nearly correspond to the location of the cells in Figure 6(d), thus clearly showing the influence of the buoyancy generated secondary flow on the axial flow. Further evidence of this influence can be seen from the temperature profiles along the vertical and horizontal centrelines of the channel shown in Figure 9, and by a direct comparison of these profiles with the corresponding temperature profiles for the unicellular flow case shown in Figure 5.

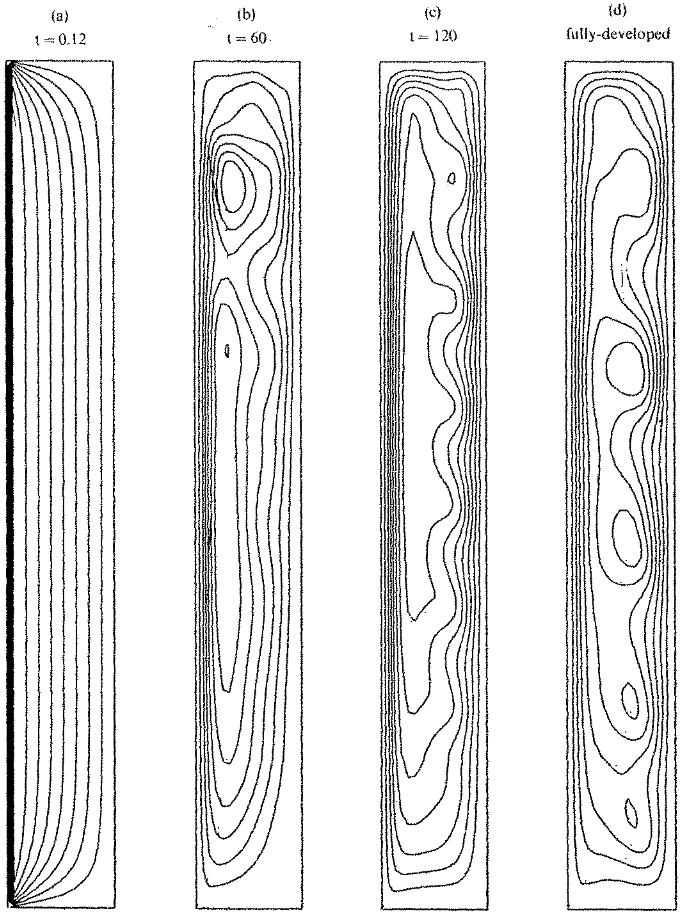

Figure 6. Contour maps of the secondary flow streamlines ($H/D = 8$, $Re = 270$, $Ra = 5{\cdot}44 \times 10^5$, $Ro = \infty$): (a) $t = 0{\cdot}12$; (b) $t = 60$; (c) $t = 120$; (d) fully-developed

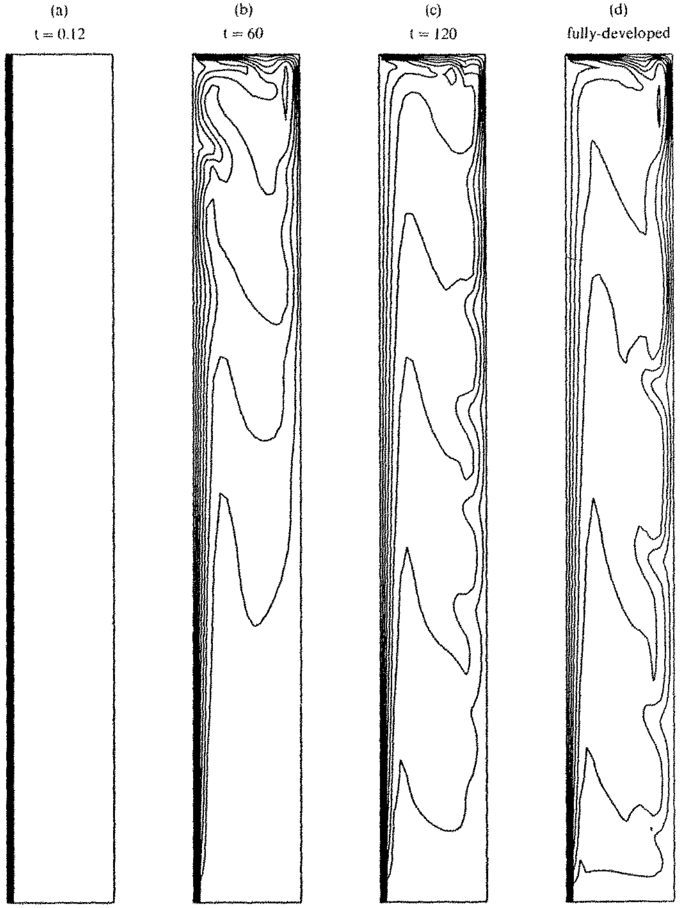

Figure 7. Contour maps of the isotherms. (Physical parameters are the same as shown in Figure 6)

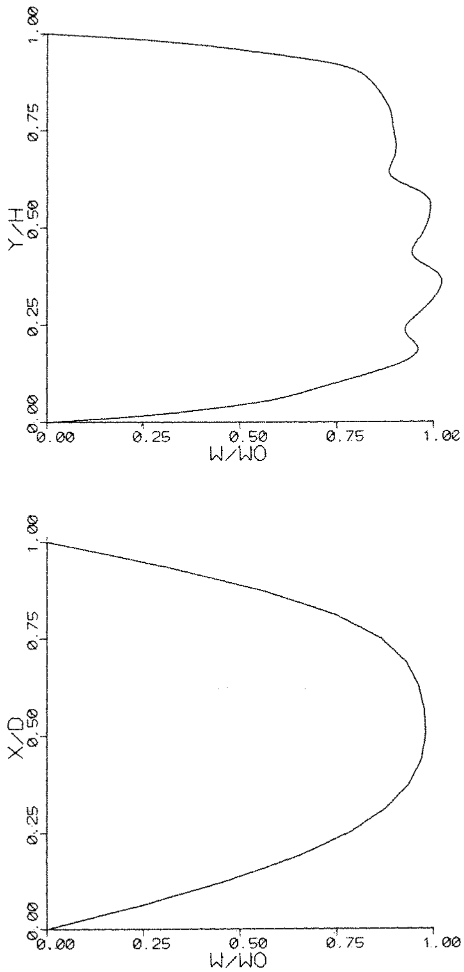

Figure 8. Fully-developed axial velocity profiles in the channel: (top) along the vertical centreline; (bottom) along the horizontal centreline

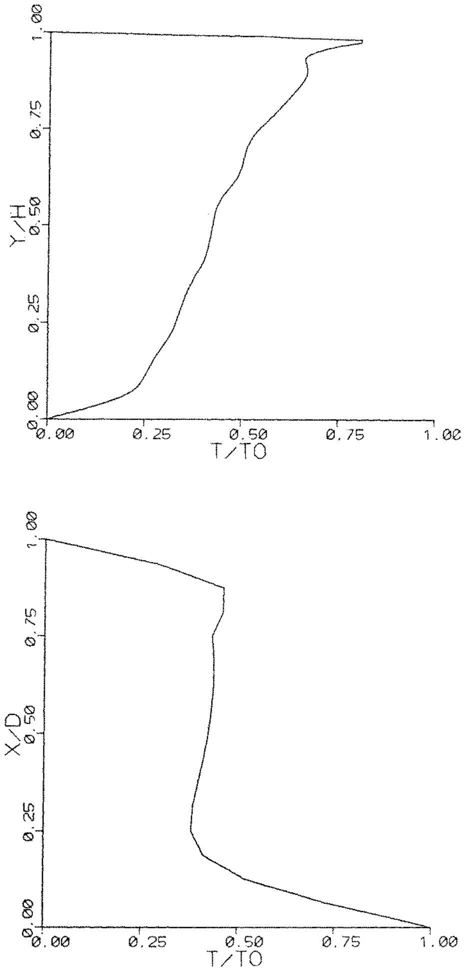

Figure 9. Fully-developed temperature profiles in the channel: (top) along the vertical centreline; (bottom) along the horizontal centreline. (Physical parameters are the same as shown in Figure 6)

We will now consider the results shown in Figures 10–25 which represent the rotating case. The results deal with two different levels of rotation rate: the first, shown in Figures 10–17, corresponds to a Rossby number of 11·5; whereas the second shown in Figures 18–25 corresponds to a Rossby number of 0·30. These values were chosen chiefly because in the related case of isothermal viscous flow in rotating channels they represent respectively the 'roll-cell' regime and the 'Taylor–Proudman' regime.[11] Similar types of secondary flows have also been predicted for isothermal viscous flow in stationary curved channels.[7] In the present work, however, the added influence of sidewall heating is being considered.

In Figures 10 and 11, the contours of the streamlines for the secondary flow and the isotherms are shown for the case when the Rayleigh number, $Ra = 1{\cdot}09 \times 10^5$ and the Rossby number, $Ro = 11{\cdot}5$. As indicated earlier, in the absence of sidewall heating (i.e. $Ra = 0$), the secondary flow at this rotation and flow rate is in the form of roll-cells aligned along the axial direction.[11] The streamlines shown in Figures 10(a)–(d) represent the flow field at different stages of evolution. As in

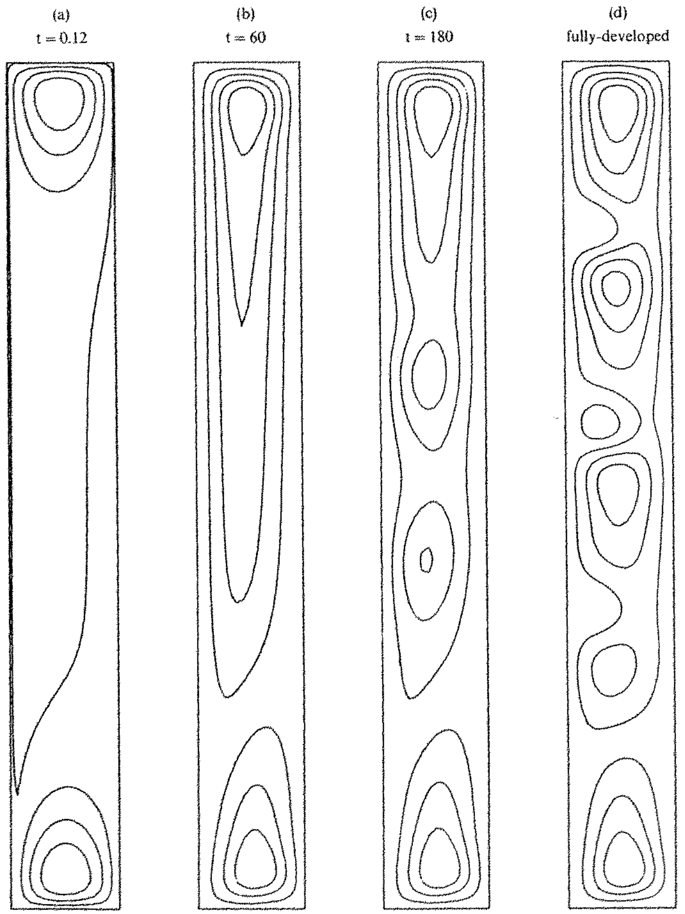

Figure 10. Contour maps of the secondary flow streamlines ($H/D = 8$, $Re = 270$, $Ra = 1{\cdot}09 \times 10^5$; $Ro = 11{\cdot}5$): (a) $t = 0{\cdot}12$; (b) $t = 60$; (c) $t = 180$; (d) fully-developed

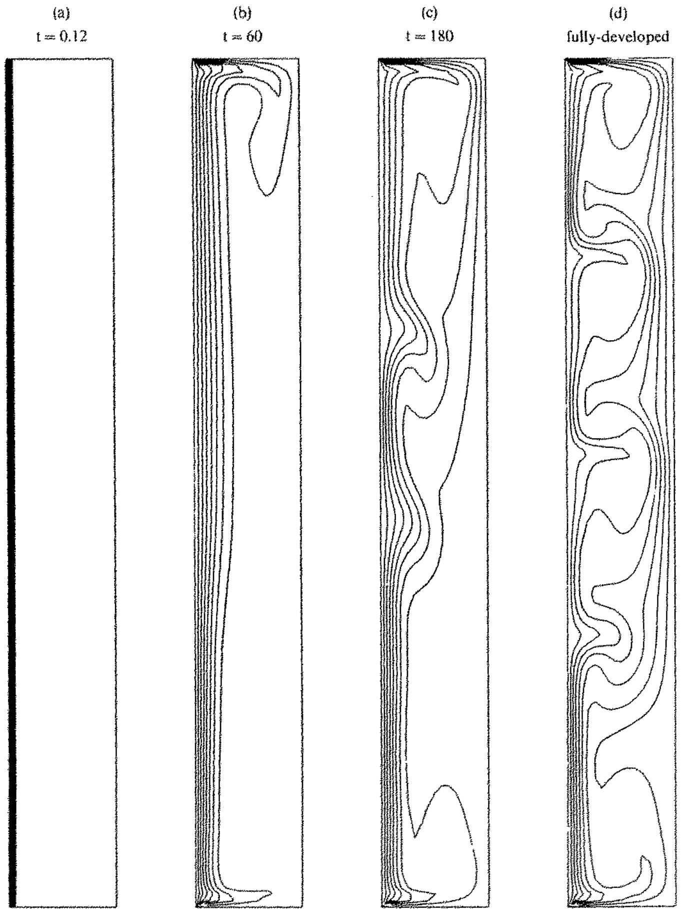

Figure 11. Contour maps of the isotherms. (Physical parameters are the same as shown in Figure 10)

the corresponding case of isothermal flow, the double-vortex secondary flow which is characteristic of channel flow with a weak rotation breaks down to a fully developed roll-cell pattern. The main difference between these two cases is that the addition of buoyancy effects, which tend to sweep the roll-cells up near the hot wall and down near the cold wall, causes a noticeable distortion in the cell shape. To observe this combined influence of sidewall heating and rotation it is instructive to consider the isotherms at different stages of evolution shown in Figures 11(a)–(d).

The influence of the buoyancy induced effect can clearly be seen by the elongated tongue of the fluid in the upper part of the channel in Figures 10(b) and 11(b). In essence, the effect of sidewall heating is to entrain the fluid from the lower portion of the channel towards the upper portion, thus causing the dislocation and distortion of the roll-cells.

In Figures 12 and 13 the axial velocity and temperature profiles along the vertical and horizontal centrelines of the channel are plotted. As anticipated, both the temperature and axial velocity profiles along the vertical centreline are highly distorted due to the presence of roll cells. However,

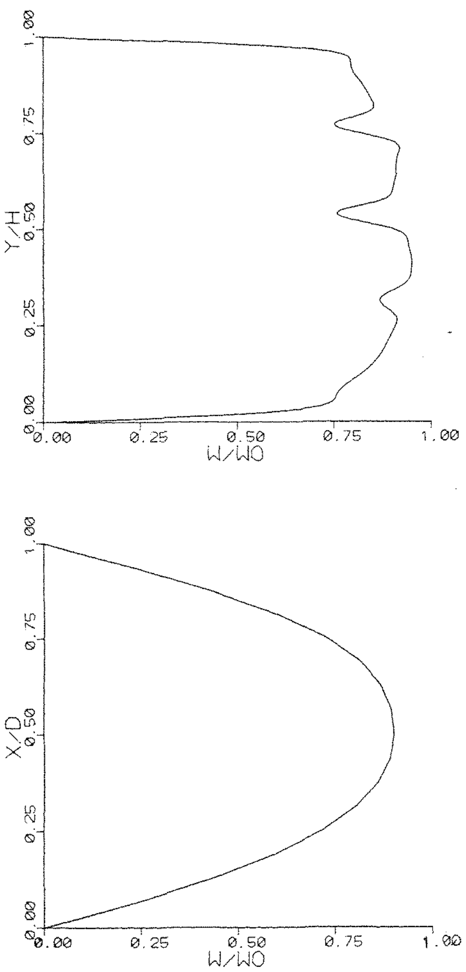

Figure 12. Fully-developed axial velocity profiles in the channel: (top) along the vertical centreline; (bottom) along the horizontal centreline

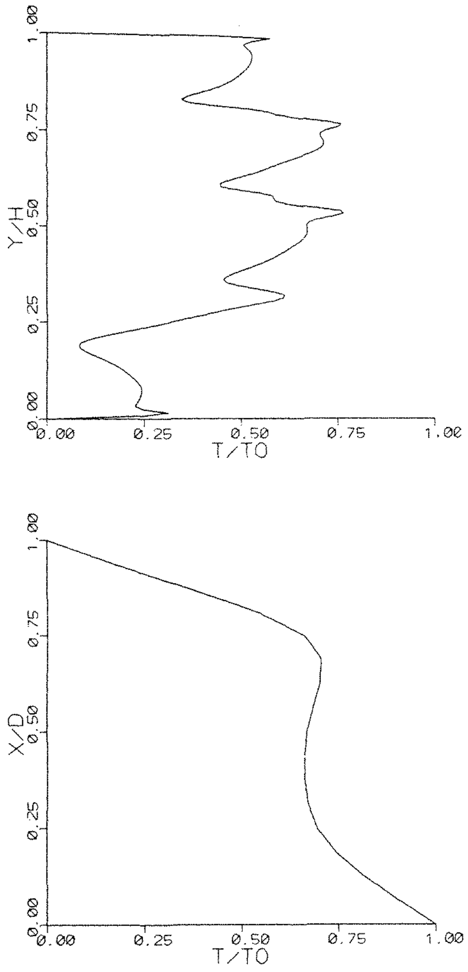

Figure 13. Fully-developed temperature profiles in the channel: (top) along the vertical centeline; (bottom) along the horizontal centreline. (Physical parameters are the same as shown in Figure 10)

the axial velocity and temperature profiles along the horizontal centreline show little distortion. In fact, the asymmetry in the axial velocity profile that is present in the corresponding isothermal case[11] (i.e. the shifting of the maximum axial velocity to the high pressure side of the channel*) is absent in this case due to the effect of buoyancy introduced by sidewall heating. In addition, an examination of the temperature and axial velocity profiles along the vertical centreline (see top parts of Figures 12 and 13) demonstrates that the troughs in the axial velocity profile correspond to the peaks in the temperature profile. This, of course, is due to the fact that the lowered axial momentum transport causes a localized enhancement of the internal energy of the fluid. Furthermore, there is a clear correlation between the peaks and troughs in the axial velocity profile (Figure 12 (top)) and the location of cells in the fully-developed secondary flow streamline contour map (Figure 10(d)). A similar correlation also exists between the temperature profile along the vertical centreline (Figure 13 (top)), the location of cells in Figure 10(d), and the location of spikes in the contour map of the isotherms of Figure 11(d).

The case of moderate rotation with moderate heating is shown in Figures 14–17. In Figures 14 and 15, the computer generated contour maps of the streamlines and isotherms are shown for a Rayleigh number of $4{\cdot}35 \times 10^5$ and Rossby number of $11{\cdot}5$. The Rayleigh number for this case is about four times larger than that for the corresponding weakly heated case discussed earlier (Figures 10–13). A comparison of the secondary flow streamlines for the weak heating and moderate heating cases shown in Figures 10(a)–(d) and 14(a)–(d) shows that when the buoyancy effects introduced by sidewall heating are stronger, the roll-cells that were formed by rotational effects are nearly eliminated due to the presence of the upwelling motion near the hot wall and the downwelling motion near the cold walls. The effect of moderate sidewall heating in this situation is essentially to introduce a buoyancy dominated secondary flow akin to that in the non-rotating case with weak sidewall heating. The axial velocity and temperature profiles along the vertical and horizontal centrelines shown in Figures 16 and 17 also confirm this statement. Here, the kinks that are present in the profiles along the vertical centreline are chiefly due to the single roll-cell near the upper wall of the channel. Indeed, when the Rayleigh number is increased further (i.e. due to enhanced sidewall heating), the flow field is found to resemble that shown in the non-rotating case with weak heating (Figures 2–5).

We will now consider the case of strong rotation, with weak sidewall heating. In Figures 18–21, the results for $Ra = 1{\cdot}09 \times 10^5$ and $Ro = 0{\cdot}30$ are shown. As indicated previously, for the rotation rate chosen, studies on isothermal viscous flows have shown that the secondary flow occurs in the form of a stretched double-vortex configuration where each vortex is compressed against the horizontal wall of the channel to which it is adjacent.[10,11] These studies have also shown that the axial velocity along the horizontal centreline of the channel is asymmetric (with its maximum velocity shifted toward the low-pressure side of the channel) and that the axial velocity profile along the vertical centreline assumes a Taylor–Proudman configuration in the interior of the channel with the exception of two peaks located near the walls of the channel.[10,11] These two peaks are thought to be generated by a mechanism akin to that of Ekman suction.[10,11] The computer generated contour maps for the secondary flow streamlines shown in Figure 18(a)–(d) clearly indicate that, for the case of weak heating, the rotational effects dominate and the fully-developed flow nearly resembles its isothermal counterpart. Examination of the contour maps of the isotherms illustrated in Figures 19(a)–(d) shows that the effects of sidewall heating leads to only a moderate distortion of the symmetry about the horizontal axis. In fact, the axial velocity profiles along the vertical and horizontal centrelines shown in Figure 20 resemble the corresponding

---

*The high pressure side of the channel, in this context, is defined as the side that is furthest from the axis of rotation.[8,11]

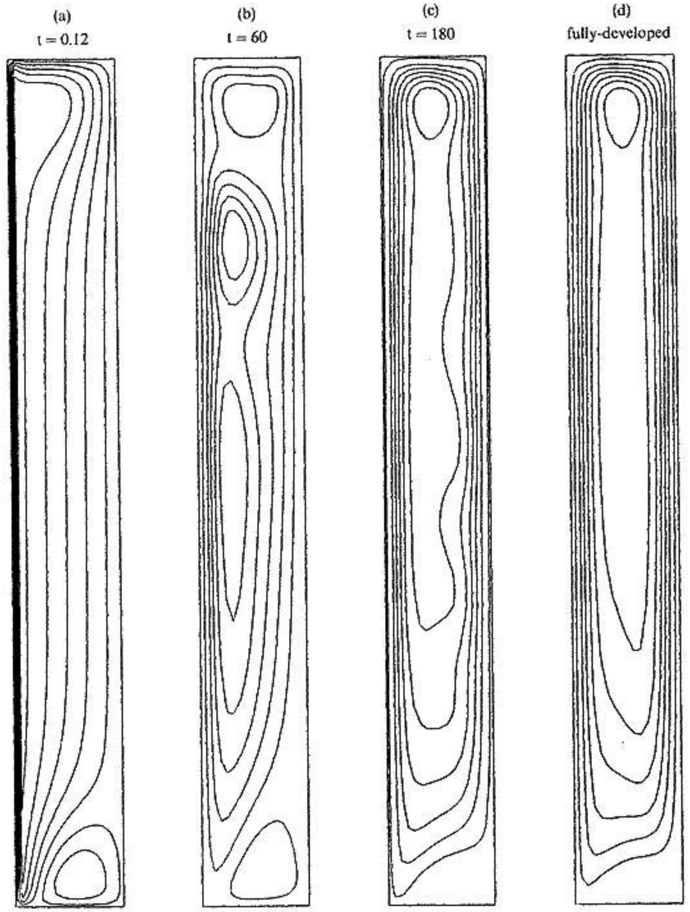

Figure 14. Contour maps of the secondary flow *streamlines* ($H/D = 8$, $Re = 270$, $Ra = 4{\cdot}35 \times 10^5$, $Ro = 11{\cdot}5$): (a) $t = 0{\cdot}12$; (b) $t = 60$; (c) $t = 180$; (d) fully-developed

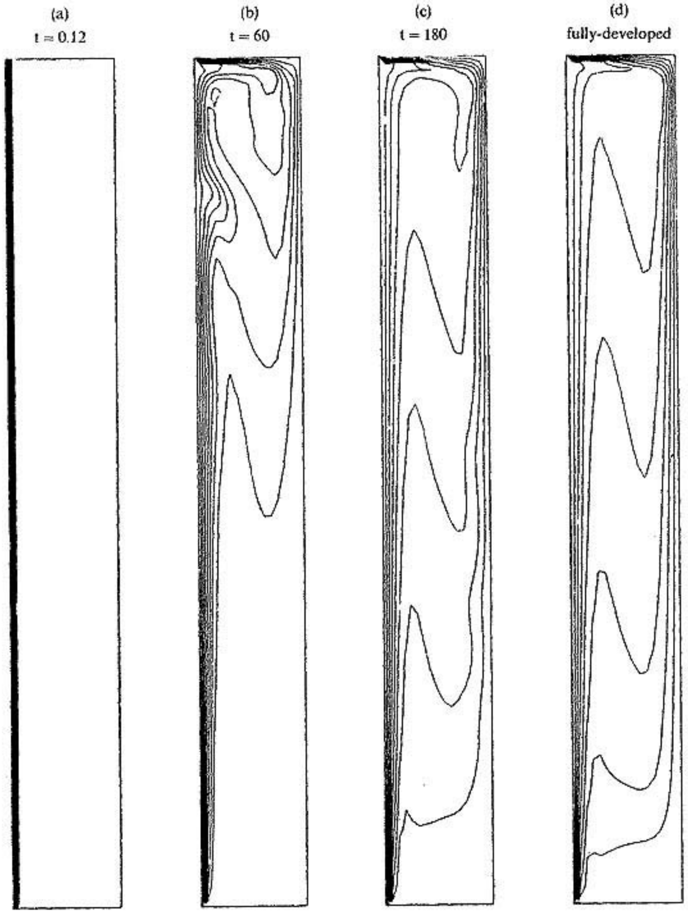

Figure 15. Contour maps of the isotherms (Physical parameters are the same as shown in Figure 14)

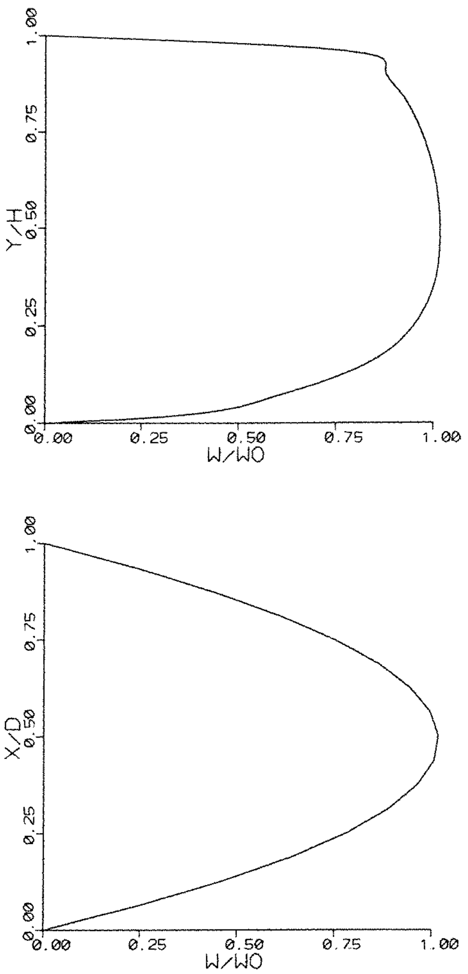

Figure 16. Fully-developed axial velocity profiles in the channel: (top) along the vertical centreline; (bottom) along the horizontal centreline

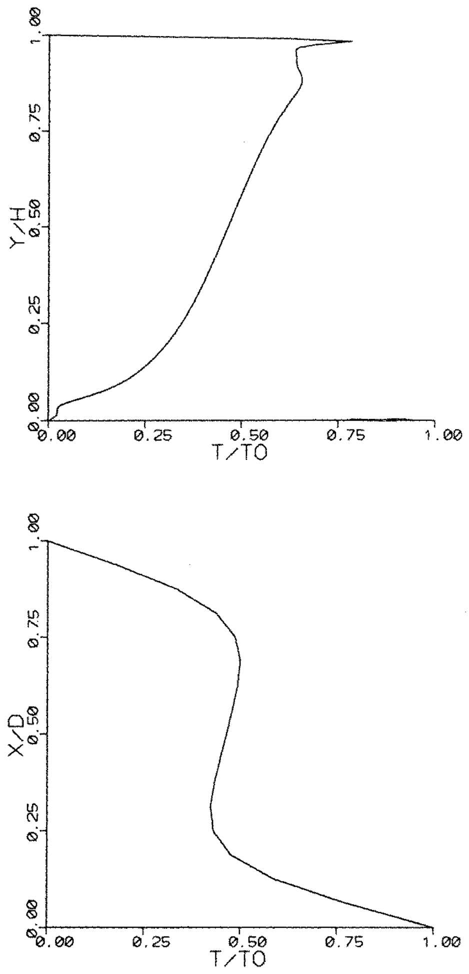

Figure 17. Fully-developed temperature profiles in the channel: (top) along the vertical centreline; (bottom) along the horizontal centreline. (Physical parameters are the same as shown in Figure 14)

profiles in the isothermal case.[10,11] In addition, it is instructive to note the large reduction in volume flux (Figure 20) similar to that in the corresponding case of isothermal viscous flow. Another interesting feature of this type of flow field is the occurrence of a thermal boundary layer near the upper and lower walls of the channel as seen from Figure 19. Here, the presence of the Ekman type layer near the boundaries subjected to a high rotation rate coupled with the temperature gradient in the boundary layer may be responsible for producing the wavy shaped structure of the isotherms. The corresponding case of thermally stratified Ekman layers has been the subject of considerable study,[6,16] and it is conceivable that a similar mechanism is responsible for the structure of the isotherms in the case under discussion. One should also note the interesting nature of the temperature profiles along the vertical and horizontal centrelines shown in Figure 21. In Figure 21 (top) we see the basic structure of the thermal boundary layer near the upper and lower boundaries as well as the drop in the internal energy (and thus, the temperature) of the fluid at the mid-section of the channel due to the presence of the secondary flow. In addition to this, the

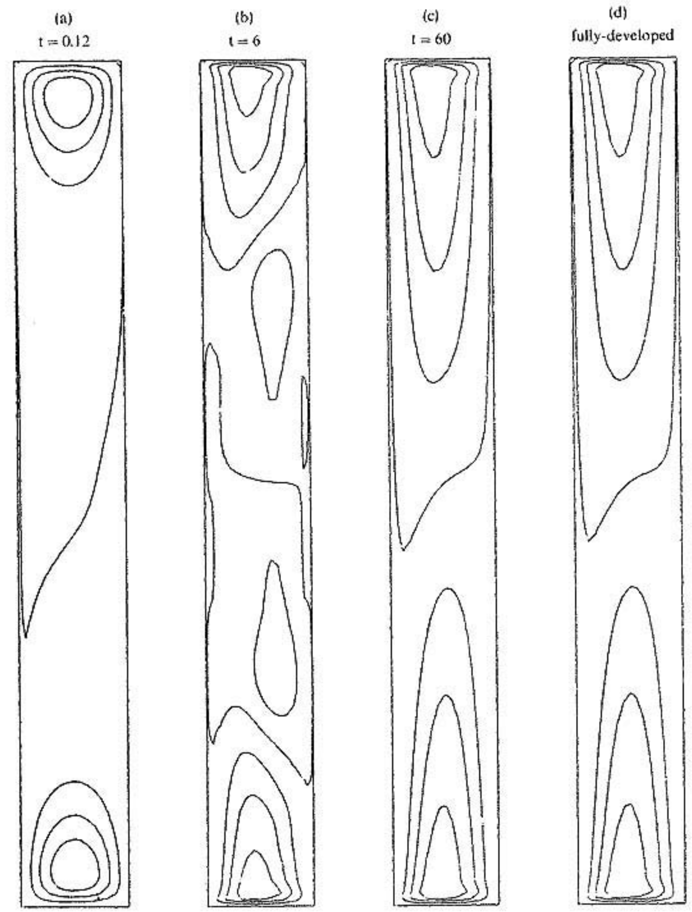

Figure 18. Contour maps of the secondary flow streamlines ($H/D = 8$, $Re = 270$, $Ra = 1{\cdot}09 \times 10^5$, $Ro = 0{\cdot}30$): (a) $t = 0{\cdot}12$; (b) $t = 6$; (c) $t = 60$; (d) fully-developed

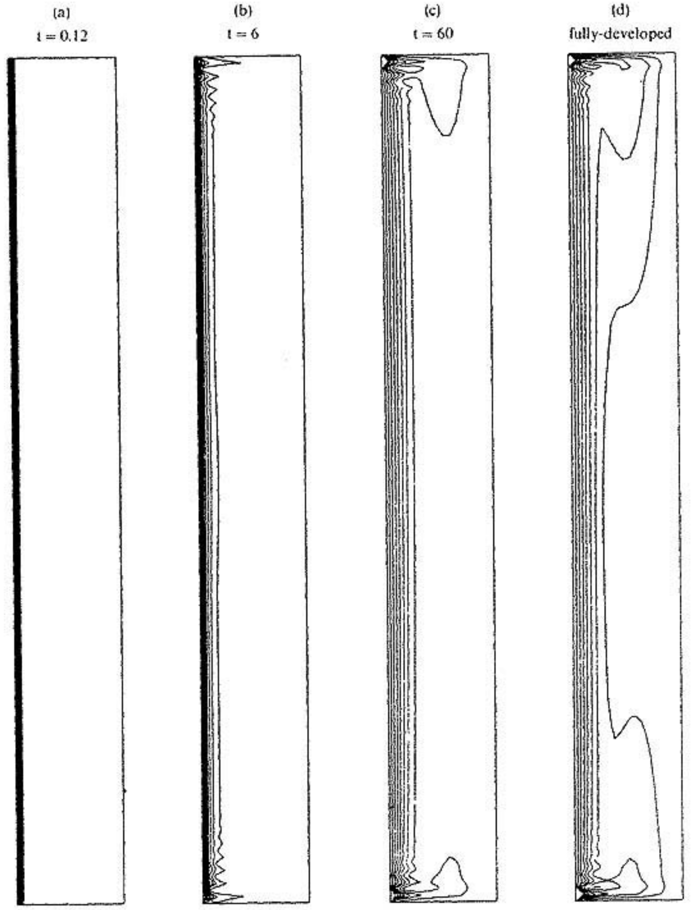

Figure 19. Contour maps of the isotherms. (Physical parameters are the same as shown in Figure 18)

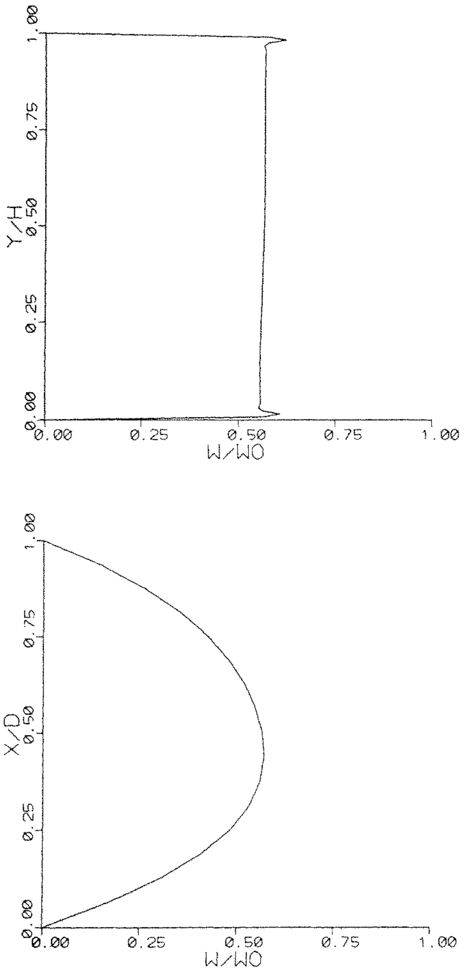

Figure 20. Fully-developed axial velocity profiles in the channel: (top) along the vertical centreline; (bottom) along the horizontal centreline.

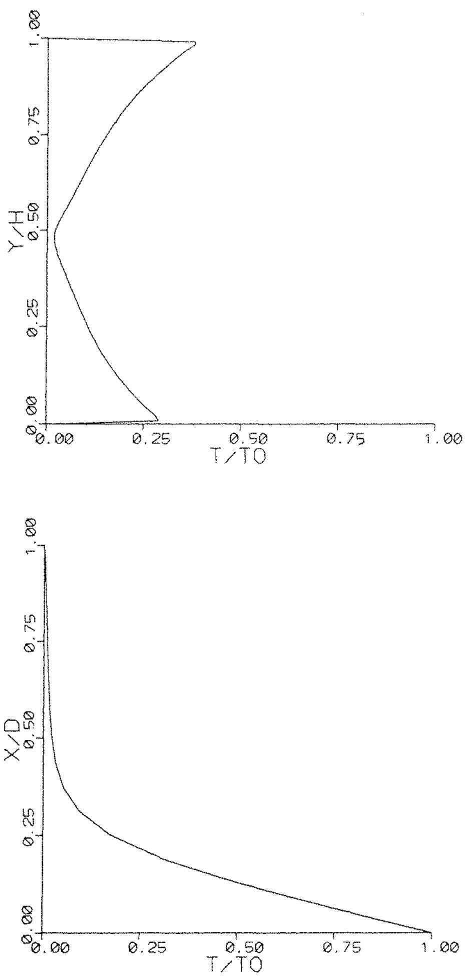

Figure 21. Fully-developed temperature profiles in the channel: (top) along the vertical centreline; (bottom) along the horizontal centreline. (Physical parameters are the same as shown in Figure 18)

effect of rotation seems to alter the nature of the lateral temperature distribution quite drastically (Figure 21 (bottom)) with very strong temperature gradients being present near the heated wall which is also the low pressure side of the channel.

The case of moderate heating at high rotation rates is considered next. The contour maps of the streamlines for the secondary flow are shown in Figure 22(a)–(d) for $Ra = 4{\cdot}35 \times 10^5$ and $Ro = 0{\cdot}30$. A comparison with the streamline structure shown in Figure 18(a)–(d) indicates that when the heating is moderate with rotation rates that are strong, the basic double vortex structure is still present; however, due to the presence of strong buoyancy forces, the vortex in the upper half of the channel is greatly enlarged. An additional indication of this distortion can be obtained by a direct comparison of the axial velocity profiles along the vertical centreline of the channel shown in the top parts of Figures (24) and (20). As one can easily see, the Taylor–Proudman configuration is distorted, and the two peaks generated by the 'Ekman suction mechanism' have appreciably different magnitudes. The effect of moderate sidewall heating can also be readily seen from the

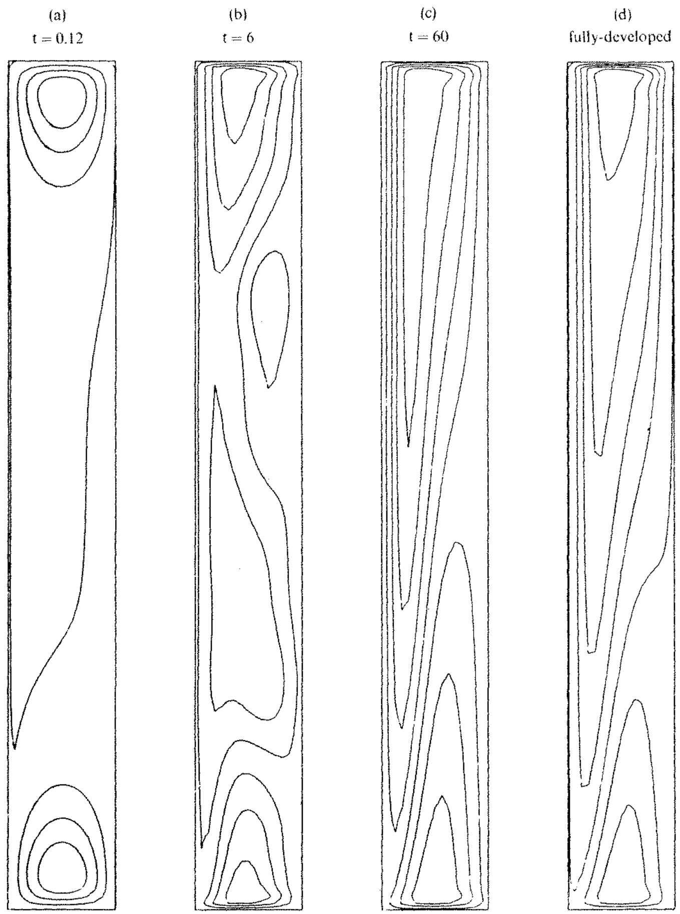

Figure 22. Contour maps of the secondary flow streamlines ($H/D = 8$, $Re = 270$, $Ra = 4{\cdot}35 \times 10^5$, $Ro = 0{\cdot}30$): (a) $t = 0{\cdot}12$; (b) $t = 6$; (c) $t = 60$; (d) fully-developed

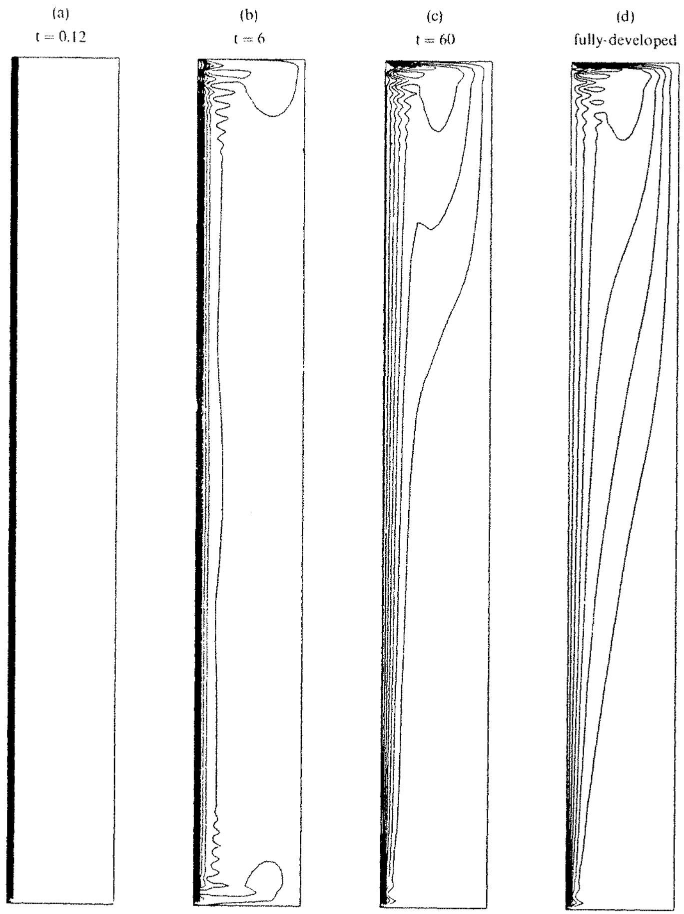

Figure 23. Contour maps of the isotherms. (Physical parameters are the same as shown in Figure 22)

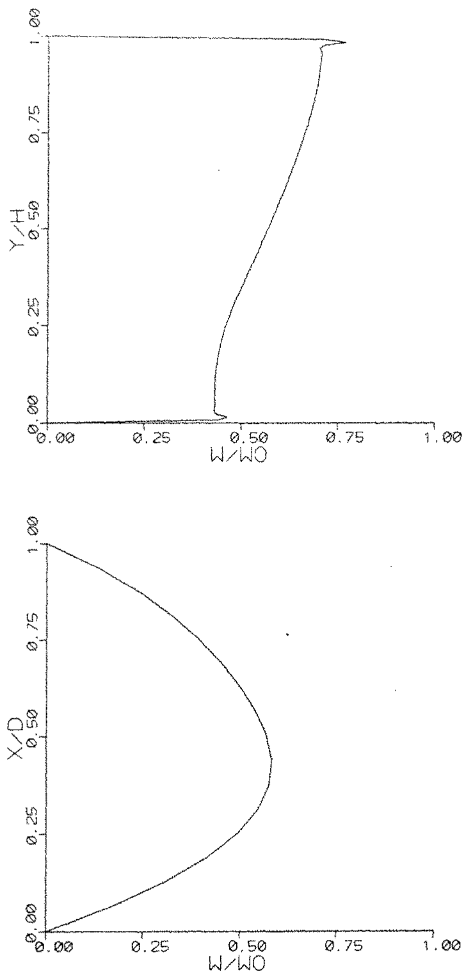

Figure 24. Fully-developed axial velocity profiles in the channel: (top) along the vertical centreline; (bottom) along the horizontal centreline

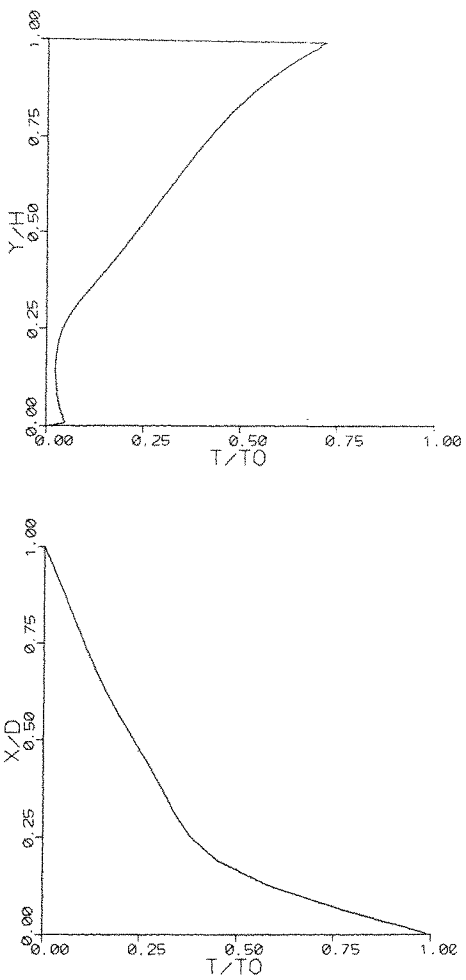

Figure 25. Fully-developed temperature profiles in the channel: (top) along the vertical centreline; (bottom) along the horizontal centreline. (Physical parameters are the same as shown in Figure 22)

contour map of the isotherms shown in Figure 23(d). A comparison with the contour map of the isotherms for the corresponding weak heating case (Figure 19(d)) clearly demonstrates the influence of the strong upwelling motion associated with the increased sidewall heating. A further evidence of this is provided in the plot of the temperature profile along the vertical centreline of the channel shown in Figure 25 (top). Another interesting feature of the increased sidewall heating is the reduction in the temperature gradient along the horizontal centreline of the channel as seen from a comparison of the bottom parts of Figures 25 and 21.

The calculation of the local and average Nusselt numbers* for the heated wall were also carried out to study the influence of the magnitude of rotation on heat transfer. The values of the average

---

*Defined as follows: $Nu = \frac{1}{H}\int_0^H \left(\frac{\partial T}{\partial x}\right)_{x=0} \mathrm{d}y$

Table I. Values of average Nusselt number for the hot wall at different values of Rossby number, *Ro*, and Rayleigh number, *Ra*. Reynolds number, $Re = 270$, $H/D = 8$ and Prandtl number, $Pr = 7$

	Ro		
Ra	∞	11·5	0·30
$1{\cdot}09 \times 10^5$	2·49	3·62	4·07
$3{\cdot}26 \times 10^5$	11·9	12·1	12·3
$4{\cdot}35 \times 10^5$	17·6	17·0	16·7
$5{\cdot}44 \times 10^5$	24·6	23·9	22·3

Nusselt number are summarized in Table I for various values of the Rossby number and Rayleigh number. As can be seen from the tabulated results, at lower Rayleigh numbers (e.g. for the case of weak sidewall heating) a decrease in the Rossby number is accompanied by an enhancement in heat transfer. This is due to the fact that the rotational forces tend to pull the fluid away from the hot wall towards the cold wall, thus augmenting the buoyancy driven transport of fluid away from the heated wall. On the other hand, at higher Rayleigh numbers, as discussed earlier, the overall heat transport is greatly increased due to the occurrence of cellular convection. We note here that for the cellular convection to occur, the presence of a strong shear layer near the vertical boundaries is needed since it is the instability induced by the shear and augmented by the lateral buoyancy force gradient that causes the formation of these cells. A decrease in Rossby number in this case tends to weaken the strength of the shear layer near the heated wall by pulling the fluid away from the wall, and thus weakening the convective transport of heat. Hence, at high Rayleigh numbers, where cellular convection is responsible for the transport of heat, a decrease in Rossby number causes a reduction in the wall Nusselt number as shown.

CONCLUSION

A numerical study has been conducted on the influence of sidewall heating in laminar pressure driven channel flow subjected to a spanwise rotation. The full non-linear time-dependent Navier–Stokes equations were solved by a finite difference method. For convenience, the value of the Reynolds number and aspect ratio were kept constant at 270 and 8, respectively, which correspond to those used by previous researchers to study isothermal viscous flow in channels.[11] The magnitude of sidewall heating used in the study has been classified either as 'moderate' or 'weak' depending on whether the classical buoyancy generated secondary flow in the form of a unicellular convective pattern broke down into a multicellular form or not. Similarly, based on the magnitude of the rotation rate, the flow field can be categorized into the following three cases: non-rotating, rotating at a moderate speed and rotating with a rapid speed. Here, the cases of moderate rotation and strong rotation refer to the flow regimes in the corresponding isothermal case where both experimentally[10] and numerically[11] the occurrence of roll-cell and Taylor–Proudman secondary flows, respectively, have been observed in the interior of the channel.

It was found that in the case of weak sidewall heating, a decrease in Rossby number leads to an increase in Nusselt number (i.e. the net heat transport) due to the lateral transport of fluid from the high temperature side to the low temperature side. On the other hand, for stationary channels with moderate sidewall heating, there is a substantial increase in the net heat transferred due to the occurrence of multicellular convection which is manifested primarily due to the presence of a strong buoyancy driven shear layer near the walls. A decrease in Rossby number in this case leads to a broadening of this buoyancy driven wall layer near the hot wall which in turn causes the cellular convective motion to weaken. Consequently, a reduction in Nusselt number takes place.

In addition, calculations have been carried out to study the influence of sidewall heating and rotational effects on the structure of the secondary flow field and the axial profiles of velocity and temperature in the channel. It was found that when the sidewall heating is weak, the flow field nearly resembles the corresponding isothermal viscous flow case. However, when the sidewall heating is moderate, depending on the magnitude of the rotation rate, different types of secondary flows were found to occur. A documentation of these streamlines along with the corresponding isotherms and profiles of axial velocity and temperature has been included.

To the best knowledge of the authors, the results presented herein represent the first calculations on the influence of sidewall heating in laminar pressure-driven viscous flow in channels subjected to a spanwise rotation. Much more research is, of course, needed to further clarify the interaction of sidewall heating and rotations in channel flow. Specifically, a detailed parametric study to relate the net heat transport to the aspect ratio of the channel, the magnitude of the axial pressure gradient, the magnitude of sidewall heating, and the magnitude of rotational speed will be quite useful. As alluded to earlier, the analysis of non-isothermal rotating flows can provide some insight into the analysis of turbomachines (as well as other rotating machinery) and in the understanding of geophysical flow systems. Furthermore, it can provide a qualitative understanding of the flow in curved channels which can also have important engineering applications. However, much more extensive research which incorporates the effects of changes in geometry, strong heating and turbulence will be needed before a thorough understanding of these engineering problems can be achieved.

REFERENCES

1. T. V. Nguyen, I. L. Maclaine-Cross and G. de Vahl Davis, 'Combined forced and free convection between parallel plates', in *Numerical Methods in Thermal Problems*, Pine Ridge Press, U.K., 1979, pp. 269–278.
2. K. J. Kennedy and A. Zebib, 'Combined free and forced convection between horizontal parallel planes: some case studies', *Int. J. Heat Mass Transfer*, **26**, 471–474 (1983).
3. J. T. Dakin, M. W. Horner, A. J. Piekarski and J. Triandafyllis, 'Heat transfer in the rotating blades of a water-cooled gas turbine', *General Electric Report No. 78CRD150* (1978).
4. D. E. Metzger, Z. X. Fan and W. B. Shepard, 'Pressure loss and heat transfer through multiple rows of short pin fins', *Proc. 7th Int. Heat Transfer Conf., No. FC24*, Hemisphere, New York, 1982, pp. 137–142.
5. J. E. Hart, 'Finite amplitude baroclinic instability', *Ann. Rev. Fluid Mech.*, **11**, 147–172 (1979).
6. J. Pedlosky, *Geophysical Fluid Dynamics*, Springer-Verlag, New York, 1982.
7. S. C. R. Dennis and M. Ng, 'Dual solutions for steady laminar flow through a curved tube', *Q.J. Mech. Appl. Math.*, **35**, 305–324 (1982).
8. D. K. Lezius and J. P. Johnston, 'Roll-cell instabilities in rotating laminar and turbulent channel flow', *J. Fluid Mech.*, **56**, 533–557 (1976).
9. C. G. Speziale, 'Numerical study of viscous flow in rotating rectangular ducts', *J. Fluid Mech.*, **122**, 251–271 (1982).
10. J. E. Hart, 'Instability and secondary motion in a rotating channel flow', *J. Fluid Mech.*, **45**, 341–351 (1971).
11. C. G. Speziale and S. Thangam, 'Numerical study of secondary flows and roll-cell instabilities in rotating channel flow', *J. Fluid Mech.*, **130**, 377–395 (1983).
12. J. E. Hart, 'Stability of the flow in a differentially heated inclined box', *J. Fluid Mech.*, **47**, 547–576 (1971).
13. G. K. Batchelor, *Introduction to Fluid Dynamics*, Cambridge University Press, 1967.
14. P. J. Roache, *Computational Fluid Dynamics*, Hermosa Publishers, 1972.
15. O. Buneman, 'A compact non-iterative poisson solver', *Stanford University Institute for Plasma Research Rep. SUIPR No. 294*, 1969.
16. R. E. Kaylor and A. J. Faller, 'Instability of the stratified Ekman boundary layer and the generation of internal waves', *J. Atmos. Sci*, **29**, 497–509 (1972).